

## Article

# Comparative Analysis of the Hydrodynamic Performance of Arc and Linear Flapping Hydrofoils

Ertian Hua <sup>1,\*</sup>, Wenchao Zhu <sup>1</sup>, Rongsheng Xie <sup>1,2</sup>, Zhongxin Su <sup>1</sup>, Haitao Luo <sup>1</sup> and Linfeng Qiu <sup>1</sup>

<sup>1</sup> College of Mechanical Engineering, Zhejiang University of Technology, Hangzhou 310023, China; 2112102394@zjut.edu.cn (W.Z.); xrspump@163.com (R.X.); suzhongxin\_66@163.com (Z.S.); haitaoluo0710@163.com (H.L.); 2112102093@zjut.edu.cn (L.Q.)

<sup>2</sup> School of Mechanical & Automotive Engineering, Zhejiang University of Water Resources and Electric Power, Hangzhou 310018, China

\* Correspondence: het@zjut.edu.cn; Tel.: +86-135-8811-4369

**Abstract:** In order to improve the hydrodynamic performance of flapping hydrofoils and solve the problem of insufficient hydrodynamic force in plain river network areas, in this study, we consider the more realistic swing of fish tails and propose an arc flapping method, the coupled motion of which has three degrees of freedom: heave, pitch, and lateral displacement. Two flapping methods, positive arcs and negative arcs, were derived on the basis of the lateral displacement direction. By using the finite volume method (FVM) and overlapping grid technology, a numerical simulation was conducted to compare and analyze the pumping performance of three types of flapping hydrofoil, namely, linear, positive arcs, and negative arcs, in order to further provide guidance for the structural optimization of bionic pumping devices. The results showed that the wake vortex structures of the three flapping modes all had anti-Kármán vortex streets, but the wake vortex of linear flapping deflected upward, and the wake vortex of positive arc flapping tended to be further away in the flow field. In one cycle, thrust was always generated by the positive arc flapping hydrofoil and the linear flapping hydrofoil, but the thrust coefficient curve of the positive arc flapping hydrofoil was more stable than that of the linear flapping hydrofoil, and the peak value was reduced by 46.5%. In addition, under the conditions of a flow rate of  $750 \text{ L}\cdot\text{s}^{-1}$  and an average head of 0.006 m, the pumping efficiency of the positive arc flapping hydrofoil reached 35%, thus showing better pumping performance than the traditional linear flapping hydrofoil under conditions with ultra-low head.

**Keywords:** flapping mode; flapping hydrofoil; pumping performance; numerical simulation; ultra-low head



**Citation:** Hua, E.; Zhu, W.; Xie, R.; Su, Z.; Luo, H.; Qiu, L. Comparative Analysis of the Hydrodynamic Performance of Arc and Linear Flapping Hydrofoils. *Processes* **2023**, *11*, 1579. <https://doi.org/10.3390/pr11051579>

Academic Editor: Lijian Shi

Received: 19 April 2023

Revised: 15 May 2023

Accepted: 17 May 2023

Published: 22 May 2023



**Copyright:** © 2023 by the authors. Licensee MDPI, Basel, Switzerland. This article is an open access article distributed under the terms and conditions of the Creative Commons Attribution (CC BY) license (<https://creativecommons.org/licenses/by/4.0/>).

## 1. Introduction

With the rapid development of industrialization and urbanization, problems in the aquatic environment and related to aquatic ecology have become increasingly prominent, especially in plain river network areas, where the problem regarding the lack of hydrodynamic force is particularly prominent [1,2]. Water diversion and drainage projects based on pump-gate joint dispatching technology have achieved some progress towards increasing the hydrodynamic force with the aim of improving water quality, but in scenarios with almost zero head, considerable problems arise, such as serious cavitation, excessive vibration, and low efficiency [3–7]. It has been found that flapping hydrofoils—bionic water pumping devices that imitate the swing of fish tails—have many advantages, such as low resistance, low noise, a low working head, and environmental friendliness [8–10], and are better able to meet the requirements for improving hydrodynamics in small river basins with an ultra-low head.

Many scholars have conducted in-depth research on flapping hydrofoils. For example, in terms of parameters, Koochesfahani found that the flapping frequency affects the vortex structure of the wake [11]. Cao et al. combined the leading edges and trailing edges of

airfoils with different thicknesses into a hybrid airfoil and found that the hybrid airfoil had a higher thrust coefficient [12]. Tian et al. found, through experiments, that the position of the pitching fulcrum of the pitching hydrofoil had a considerable influence on the evolution of the wake vortex of the hydrofoil [13]. In addition, in terms of applications, they have been widely used in underwater thrusters [14], gliders [15,16], energy harvesting devices [17–19], and valveless piezoelectric pumps [20,21]. In addition, in order to explore ways of achieving improved hydrodynamic performance of hydrofoils, research on the use of a flapping mode in hydrofoils is an indispensable part. A. Andersen et al. found, using the soap film technique, that the wake diagrams for pure heave and pure pitch motions are qualitatively similar [22]. Abbaspour and Song conducted research using three flapping modes—pure pitch, pure heave, and coupled heave–pitch—by means of experiments and numerical calculations, and concluded that an anti-Kármán vortex street always appears in the wake when employing coupled heave–pitch motion [23–25]. On this basis, Du et al. further subdivided the flapping mode employing coupled heave–pitch motion, and compared the propulsion performance of the four resulting flapping modes, concluding that the greatest average thrust occurs when the maximum pitch angle is at the initial position and the pitch direction is the same as the heave direction, and no resistance is generated [26]. On the basis of the flexibility of a fish’s body, Feng et al. established a hydrofoil model with fish-like flapping (fish-like mode; FM) and found that the induced effect of the wake vortex was enhanced and the speed in the y direction increased with increasing lateral amplitude of the FM hydrofoil [27]. Ma et al. proposed a pendulous flapping hydrofoil model and analyzed the influence of different motion parameters on the hydrofoil’s mechanical performance in terms of the change in the angle of attack and the vortex structure of the hydrofoils through numerical simulations [28]. Lu and Boudis examined different non-sinusoidal flapping models by changing the adjustable parameter  $K$ , and a strong anti-Kármán vortex street could be induced at a higher value of  $K$ , resulting in an increase in the thrust. In addition, it was found that the symmetry of the anti-Kármán vortex street in the wake was destroyed when employing non-sinusoidal flapping [29–31].

The research results above indicate that the flapping hydrofoil had better hydrodynamic performance under appropriate parameters, and the use of different flapping modes has a significant impact on the hydrodynamic performance of the hydrofoil. However, currently, the heave direction of the flapping hydrofoil is generally linear motion, while fish use an arc motion to achieve propulsion using its body/caudal fin (body and/or caudal fin; BCF) [32,33]. Therefore, with reference to a more realistic fish tail swing, we propose an arc flapping method. We utilize the finite volume method (FVM) and overlapping grid technology to compare and analyze the influence of the use of an arc flapping hydrofoil versus a linear flapping hydrofoil on water propulsion via numerical simulation, and this research provides further guidance for the structural optimization of bionic pumping devices.

## 2. Motion Model

### 2.1. Motion Description

The traditional flapping mode used by flapping hydrofoils is linear flapping, which is a compound motion with two degrees of freedom in which a pitching motion and a heaving motion are coupled. Arc flapping is a movement mode based on linear flapping that adds a lateral movement direction, as shown in Figure 1. The lateral direction has positive and negative points, so the arc flapping can be divided into positive arc flapping and negative arc flapping. Arc flapping was the main research focus of this study. Figure 2 presents a schematic diagram of the movement of the three flapping modes in a single period.

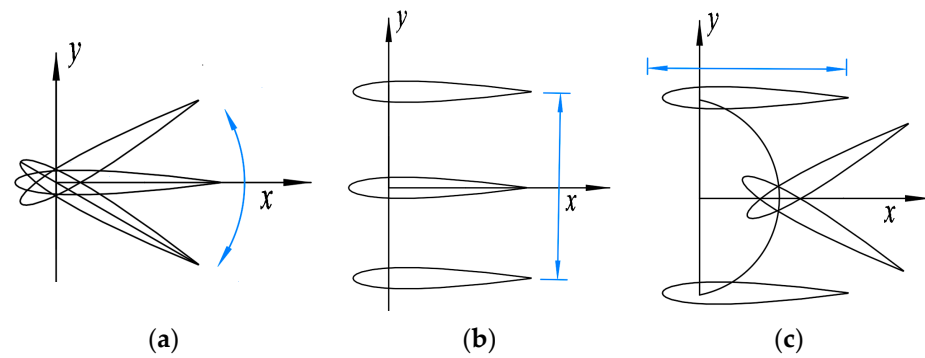


**Figure 1.** Schematic diagrams of motion in three degrees of freedom. (a) Pitching motion; (b) heaving motion; (c) lateral motion.

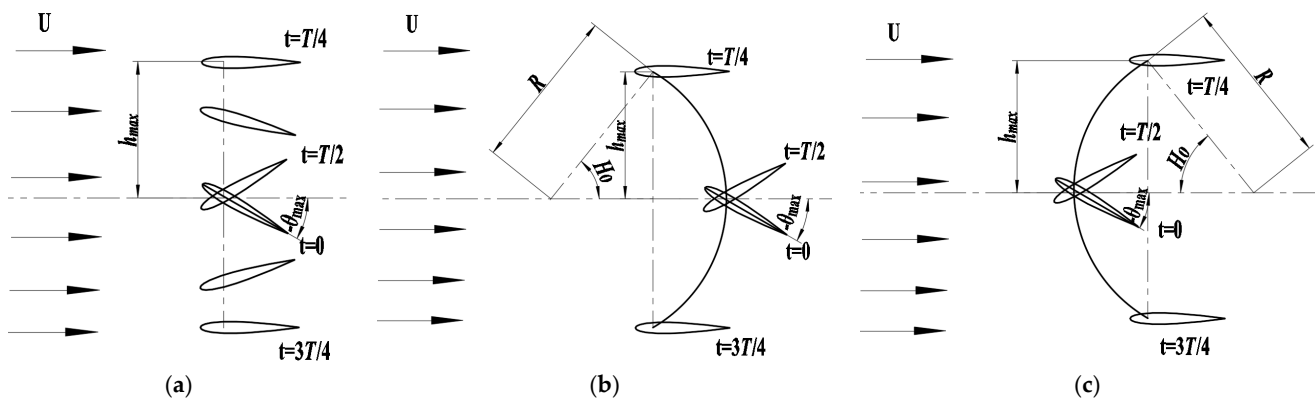


**Figure 2.** Schematic diagram of the three flapping modes: (a) linear flapping; (b) positive arc flapping; (c) negative arc flapping.

In Figure 2,  $h_{max}$  represents the heaving amplitude of the flapping hydrofoil,  $\theta_{max}$  represents the pitch amplitude of the flapping hydrofoil,  $H_0$  represents the heave angle of the flapping hydrofoil,  $R = h_{max} / \sin(H_0)$  is the radius of curvature of the arc flapping, and  $T$  represents the period of motion. The equation for the motion of a linear flapping hydrofoil is

$$\begin{cases} y(t) = h_{max} \sin(2\pi ft) \\ \theta(t) = \theta_{max} \sin(2\pi ft - \varphi) \end{cases} \quad (1)$$

The equation for the motion of an arc flapping hydrofoil is

$$\begin{cases} x(t) = (-1)^n (R \cos(H_0 \sin(2\pi ft)) - R) \\ y(t) = R \sin(H_0 \sin(2\pi ft)) \\ \theta(t) = \theta_{max} \sin(2\pi ft - \varphi) \end{cases} \quad (2)$$

where  $x(t)$  and  $y(t)$  are the displacements of the hydrofoil in the yaw direction and the heave direction, respectively;  $\theta(t)$  is the pitch displacement of the hydrofoil;  $n$  is a variable parameter, which is a positive arc flapping equation when  $n$  is 0, and a negative arc flapping equation when  $n$  is 1;  $\omega = 2\pi f$  is the angular velocity;  $f = 1/T$  is the flapping frequency of the hydrofoil, where the heave frequency, pitch frequency, and yaw frequency are considered to be equal; and  $\varphi$  is the phase difference in the pitch, yaw, and heave motions. The velocity equation of the flapping hydrofoil is obtained by taking the derivative of the equation of motion described above:

$$\begin{cases} \dot{x}(t) = \frac{dx(t)}{dt} \\ \dot{y}(t) = \frac{dy(t)}{dt} \\ \dot{\theta}(t) = \frac{d\theta(t)}{dt} \end{cases} \quad (3)$$

where  $\dot{x}(t)$  is the yaw speed of the flapping hydrofoil,  $\dot{y}(t)$  is the heave speed of the flapping hydrofoil, and  $\dot{\theta}(t)$  is the pitch speed of the flapping hydrofoil.

In this study, NACA0012 was used as a model for the flapping hydrofoil, as shown in Figure 3, with the following parameters: chord length  $c = 0.3$  m; span  $s = 1$  m; distance between the position of the pivot of the hydrofoil and leading edge  $l = 0.2c$ ; fixed heave amplitude  $h_{\max} = 0.5c$ ; pitch amplitude  $\theta_{\max} = \pi/6$  rad; heave angle  $H_0 = \pi/3$  rad; phase angle  $\varphi = \pi/2$  rad; and flapping frequency  $f = 1$  Hz. The Strouhal number was defined as  $St = 2f A_{\max}/\bar{U}$ , where  $\bar{U}$  is the average value of the outlet velocity after the flow has stabilized.

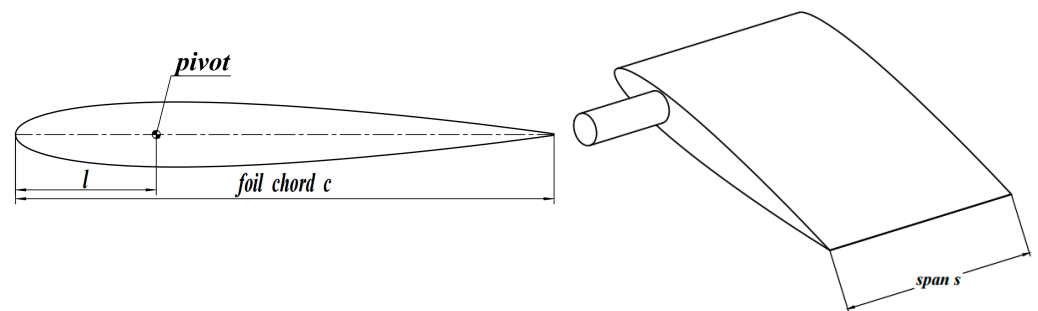


**Figure 3.** Schematic diagram of the hydrofoil.

## 2.2. Mechanical Parameters and Pumping Indicators

In order to be able to conveniently study the performance of the flapping hydrofoil, the instantaneous thrust  $F_T(t)$  and the instantaneous lift  $F_L(t)$  generated by the hydrofoil need to be transformed, without dimensions, to obtain the following parameters.

Instantaneous thrust coefficient of the flapping hydrofoil:

$$C_T(t) = \frac{2F_T(t)}{\rho \bar{U}^2 s c}, \quad (4)$$

Instantaneous lift coefficient of the flapping hydrofoil:

$$C_L(t) = \frac{2F_L(t)}{\rho \bar{U}^2 s c}, \quad (5)$$

Average thrust coefficient of the flapping hydrofoil:

$$\bar{C}_T = \frac{1}{T} \int_t^{t+T} C_T(t) dt, \quad (6)$$

Average lift coefficient of the flapping hydrofoil:

$$\bar{C}_L = \frac{1}{T} \int_t^{t+T} C_L(t) dt, \quad (7)$$

The angle of attack, which is the angle between the equivalent incoming velocity and the chord of the wing (as shown in Figure 4) is an important factor affecting the performance of the flapping hydrofoil.

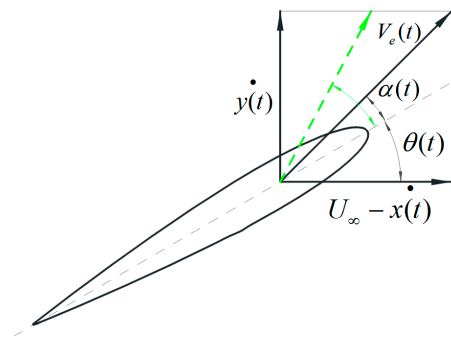


**Figure 4.** Schematic diagram of the angle of attack of the hydrofoil.

The equivalent incoming flow velocity is defined as

$$V_e(t) = \sqrt{(U_\infty - \dot{x}(t))^2 + \dot{y}(t)^2}, \quad (8)$$

The angle of attack is defined as

$$\alpha(t) = \arctan \frac{-\dot{y}(t)}{U_\infty - \dot{x}(t)} - \theta(t), \quad (9)$$

where  $U_\infty$  is the incoming flow velocity.

The average power provided to the flapping hydrofoil during one period of motion is defined as

$$\overline{P}_{in} = \frac{1}{T} \left( \int_t^{t+T} F_T(t) \dot{x}(t) dt + \int_t^{t+T} F_L(t) \dot{y}(t) dt + \int_t^{t+T} M(t) \dot{\theta}(t) dt \right), \quad (10)$$

In order to further study the pumping performance of the flapping hydrofoil, the performance parameters flow rate, head, and pumping efficiency of the flapping hydrofoil were derived. The specific formulas were as follows:

The outlet average flow rate of a steady flow field is defined as

$$\overline{Q} = \overline{U}bs, \quad (11)$$

The average head of a flapping hydrofoil is defined as

$$\overline{H} = \frac{\Delta \overline{P}}{\rho g}, \quad (12)$$

The pumping efficiency of a flapping hydrofoil is defined as

$$\eta = \frac{\Delta \overline{P} \cdot \overline{Q}}{\overline{P}_{in}}, \quad (13)$$

where  $\rho$  is the fluid's density;  $M(t)$  is the instantaneous driving torque about the pivot to which the hydrofoil is subjected during motion;  $b$  is the width of the river channel, taken to be 0.8 m; and  $\Delta \overline{P}$  is the average pressure difference between the inlet and the outlet.

### 3. Numerical Method and Validation

#### 3.1. Governing Equation and Turbulence Model

On the basis of the finite volume method (FVM), this study used the CFD (computational fluid dynamics) simulation software package FLUENT 2020 from ANSYS Corporation in the United States to perform the numerical simulation. The Reynolds time-averaged

mass conservation equation and Reynolds time-averaged momentum conservation equation were used to capture the characteristics of a two-dimensional incompressible turbulent flow field. Therefore, the governing equations can be expressed as follows.

$$\frac{\partial \bar{u}_i}{\partial x_i} = 0, \quad (14)$$

$$\frac{\partial \bar{u}_i}{\partial t} + \bar{u}_j \frac{\partial \bar{u}_i}{\partial x_j} = -\frac{1}{\rho} \frac{\partial \bar{p}}{\partial x_i} + \frac{\partial}{\partial x_j} [(\gamma + \gamma_t) \left( \frac{\partial \bar{u}_i}{\partial x_j} + \frac{\partial \bar{u}_j}{\partial x_i} \right)], \quad (15)$$

where  $\bar{u}_i$  ( $i = 1, 2$ ) is the fluid's average velocity,  $x_i$  ( $i = 1, 2$ ) is the space coordinate,  $P$  is the fluid's pressure,  $\gamma$  is the kinematic viscosity coefficient,  $\gamma_t = c_\mu k^2 / \varepsilon$  is the turbulent viscosity coefficient,  $k$  is the turbulent kinetic energy,  $\varepsilon$  is the dissipation rate of the turbulent energy, and  $c_\mu$  is a constant.

During the movement of the flapping hydrofoil, the leading edge and the trailing edge of the hydrofoil generate, move, and shed vortices. The realizable  $k - \varepsilon$  turbulence model is able to capture the information of the complex flow field well, and is particularly suitable for describing the complex flow fields associated with the generation and shedding of vortices, and the computational cost is moderate. Therefore, the realizable  $k - \varepsilon$  turbulence model was used to solve the N-S equation in this study, and the corresponding equation was described in [26].

### 3.2. Computational Domain and Mesh Generation

In order to utilize the computational resources reasonably and avoid the problem of negative volume, the overlapping grid technique was used to solve the problem of the flapping hydrofoil's motion. In order to fully develop a wake vortex and consider the influence of the two banks of the river on the flow field, the overall calculation domain was set to  $5 \times 0.8$  m. The computational domain consisted of a moving foreground grid and a stationary background grid, as shown in Figure 5. The foreground grid was a hybrid grid, and the area near the hydrofoil surface was densified. The background grid was composed of a structured grid with a global size of 0.008 m. During the numerical calculation of the two sets of grids, the area corresponding to the foreground grid in the background grid was deleted first, and then the data of the adjacent grid cells were transferred by interpolation. Therefore, the global size of the foreground grid and of the background grid were set to be the same to improve the calculation accuracy.

Because there was a large gradient of normal velocity near the wall, in order to better capture the flow field on the wall, it was necessary to establish boundary layers on the hydrofoil and the wall of the channel, as shown in Figure 5. In this study, the height of the first layer of the boundary layer on the hydrofoil wall was set as  $4 \times 10^{-6}$  m, and the calculated  $Y^+$  was  $< 1$ .

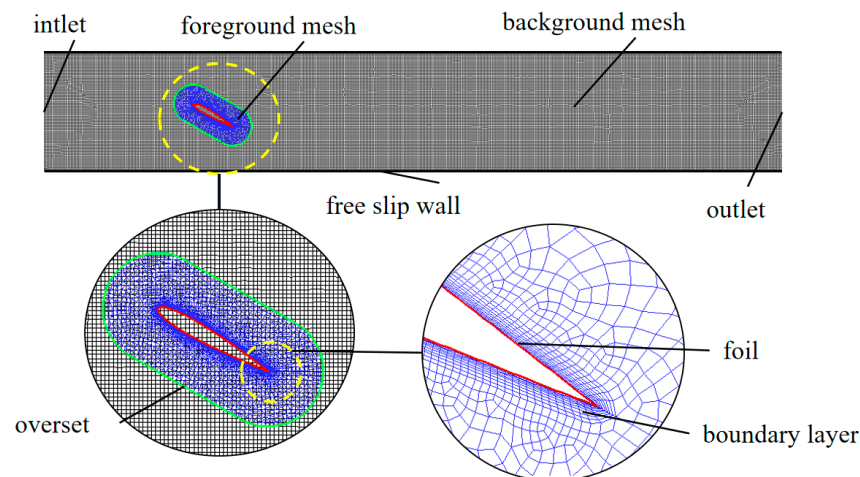


**Figure 5.** Computational domain and grid partitioning.

### 3.3. Boundary Conditions and Parameter Settings

In this study, the boundary conditions were set as the pressure of the inlet and the pressure of the outlet in order to simulate a real dead water environment. The outermost boundary line of the foreground grid was set as the overset, and the hydrofoil surface and the walls on both sides were set as free slip walls.

In the solution settings, a transient solver was selected, and the coupled algorithm was adopted as the pressure coupling equation. The turbulent kinetic energy equation and turbulent dissipation rate were discretized by the first-order upwind scheme, and the momentum equation was discretized using the second-order upwind scheme. After the mesh, boundary conditions and parameter settings had been generated, calculations regarding the flapping hydrofoil could be carried out.

### 3.4. Verification of the Independence of the Grid Number and Time Steps

In the process of CFD numerical calculation, because the grid's density and time step have a direct impact on the results of the numerical calculation and the calculation speed, we verified the independence of the grid number and the time step in order to make the calculation results more accurate and reliable. The working conditions for the verification were as follows: inlet flow rate,  $U = 0.4$  m/s; pitch amplitude,  $\theta_{\max} = 30^\circ$ ; heave amplitude,  $h_{\max} = 0.15$  m; flapping frequency,  $f = 1$  Hz.

To verify the independence of the grid number, we selected three sets of grids of 7.4w, 15.5w, and 35.8w for the purposes of numerical simulation. The results are shown in Figure 6a. On the basis of this comparison, it could be seen that the instantaneous thrust coefficients of the three sets of grids were basically the same, and the differences were small. Therefore, considering computational efficiency and computing resources, the grid of 15.5w was finally selected for use in the subsequent calculations.

To verify the independence of the time steps, we selected three time steps—0.05 s, 0.01 s and 0.005 s—for use in the numerical simulation. The results are shown in Figure 6b. On the basis of this comparison, it was found that the deviation in the instantaneous thrust coefficient when the time step was 0.05 s was larger than that for the other two time steps. Therefore, considering calculation accuracy and efficiency, a time step of 0.01 s was finally selected for the subsequent calculations.

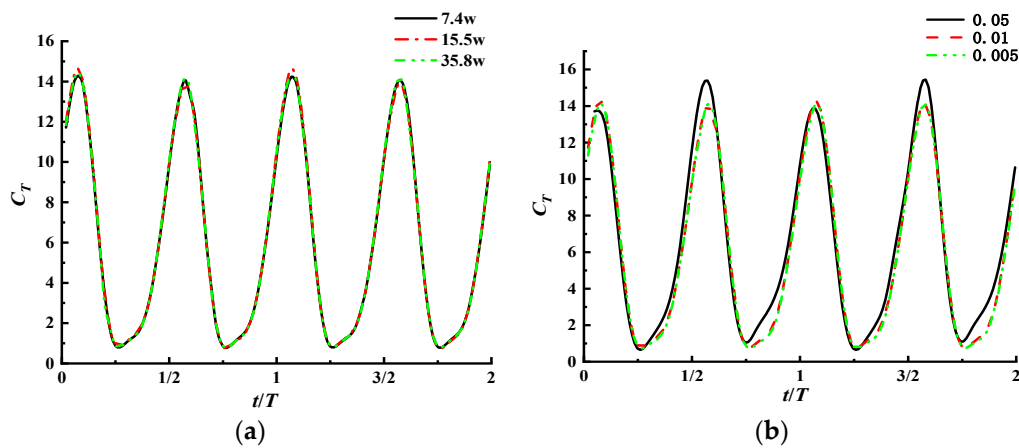


**Figure 6.** Verification of independence: (a) grid number; (b) time steps.

### 3.5. Validation

In order to verify the reliability of the numerical calculation method, in this study, it was compared with the experimental results obtained in the MIT towing tank laboratory [34]; the NACA0012 airfoil was selected, the numerical calculation model was established according to the experimental conditions described in the literature, and the simulation's parameter settings were kept consistent with the experimental conditions in the literature [34]. The size of the computational domain was  $20c \times 15c$ . The other parameters were: inlet velocity  $U = 0.4$  m/s; phase angle  $\varphi = 90^\circ$ ; maximum angle of attack  $\alpha_{\max} = 30^\circ$ ; heave amplitude and chord length of the hydrofoil  $h_{\max} = c = 0.1$  m; distance between the central pivot of the hydrofoil and the leading edge of the hydrofoil  $l = 1/3c$ ; span of the hydrofoil  $s = 0.6$  m; flapping frequency  $f = 1$  Hz. The average thrust coefficient was calculated when the Strouhal number  $St$  was 0.2, 0.3, 0.4, 0.5, and 0.6. The results are shown in Figure 7.

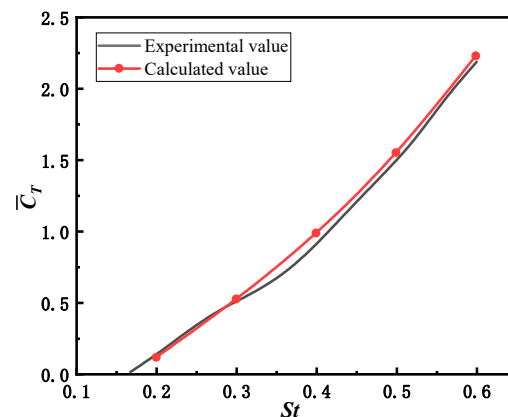


**Figure 7.** Comparison between the results of the numerical simulation and the experimental data in the literature [34].

On the basis of this comparison, it was found that the numerical calculation results were in good agreement with the experimental results, proving the numerical calculation method used in this study to be effective.

## 4. Results

### 4.1. Analysis of the Effects of Flapping Mode on the Mechanical Properties of Hydrofoils

In order to study the changes in the mechanical properties of the flapping hydrofoil in a water body with different flapping modes, a flapping frequency  $f = 1$  Hz was taken for the three flapping modes in order to carry out the numerical calculations. The instantaneous

thrust lift coefficient curves of the different flapping modes were obtained. The results are shown in Figure 8.

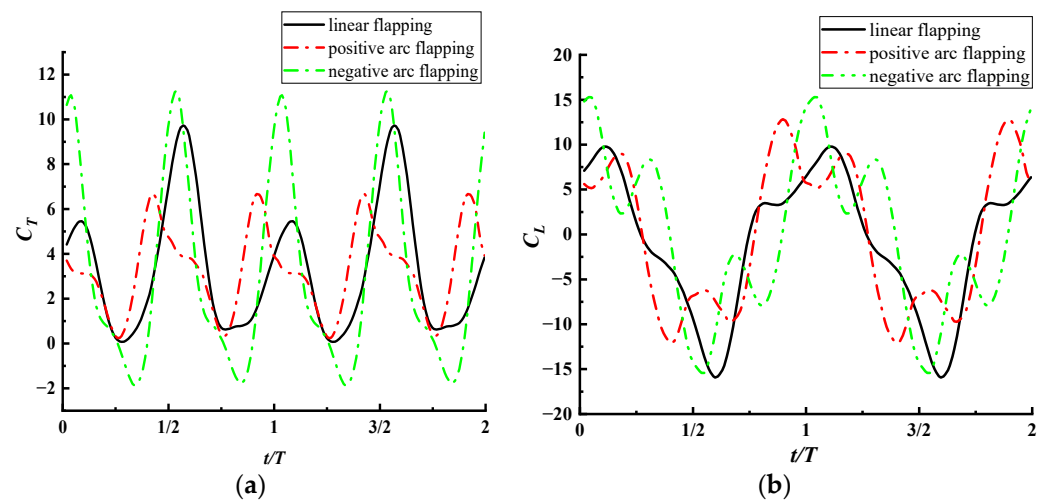


**Figure 8.** Variation in the instantaneous thrust and lift coefficients for different flapping modes: (a) instantaneous thrust coefficients; (b) instantaneous lift coefficients.

In order to facilitate a comparison, the relative values of the dimensionless time of each period were taken as the abscissa. Figure 8a shows the curves of variation in the instantaneous thrust coefficient when using different flapping modes. Referring to Figure 2b, it can be seen from the figure that for positive arc flapping, the hydrofoil started flapping upward from the initial position, and the instantaneous thrust coefficient gradually decreased. When the hydrofoil moved to the maximum heave amplitude, the instantaneous thrust coefficient reached its lowest value, almost reaching 0. Then, the hydrofoil started flapping downward in the opposite direction, and the instantaneous thrust coefficient increased continuously, reaching its peak value before returning to the initial position. Then, the instantaneous thrust coefficient decreased continuously, reaching its second valley value at the amplitude position. It then began flapping upward, resulting in an increase in the instantaneous thrust coefficient, which reached a second peak before returning to its initial position, and then the instantaneous thrust coefficient began to decrease.

On the basis of comparison, it was found that for the three flapping modes in a movement cycle, the changes in the instantaneous thrust coefficient were basically the same, with two peaks and two valleys. The difference was that, firstly, the peak of linear flapping appeared obviously later than that of the other two, while the peak of positive arc flapping appeared earliest. Secondly, the two peaks and two valleys of positive arc flapping and negative arc flapping were almost the same, but the two peaks of linear flapping were quite different. In addition, the peak value of positive arc flapping was much smaller than that of the other two flapping modes, and 46.5% lower than that of the linear flapping mode.

Figure 9 shows the nephogram of the distribution of pressure on the surface of the hydrofoil for three flapping modes at the peak position; a downward flapping motion was selected for all three. It can be seen from the figure that for the three flapping modes, the hydrofoil presented a situation where the lower surface was a high-pressure area and the upper surface was a low-pressure area. The difference was that the lower surface had a part with low pressure in positive arc flapping, and the range of the high-pressure area on the lower surface was much smaller than that of the other two flapping modes, while the range of the low-pressure area on the upper surface was equivalent to that of the other two flapping modes. Therefore, the difference in pressure between the two sides of the hydrofoil with positive arc flapping was small, which resulted in the peak value of the hydrofoil being low. From this, it can be seen that the stability of the motion of the hydrofoil

was better when using the positive arc flapping mode. Finally, positive arc flapping and linear flapping always produced thrust during the whole process of movement, while negative arc flapping produced resistance some of the time, so it can be concluded that positive arc flapping and linear flapping always produce propulsion of the water body.

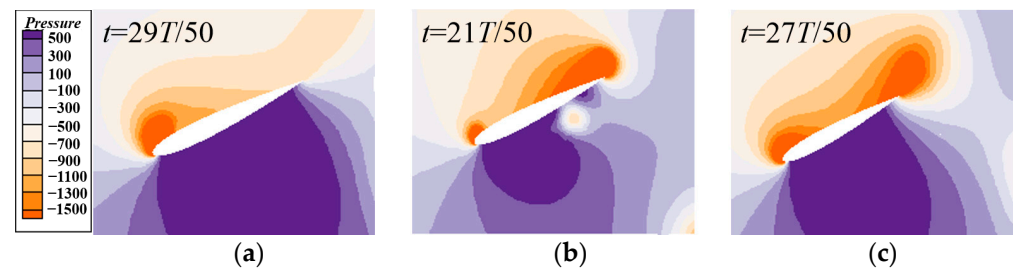


**Figure 9.** The distribution of pressure on the surface of the hydrofoil at the peak position of the three flapping modes. (a) Linear flapping; (b) positive arc flapping; (c) negative arc flapping.

It can be seen in Figure 8b that the instantaneous lift coefficients had one peak and one valley in the linear flapping mode, and there were two peaks and two valleys for the two types of arc flapping in one period, and the evolution of the curve of negative arc flapping had an obvious lag compared with positive arc flapping. In addition, the instantaneous lift coefficient curves of the two types of arc flapping were basically symmetrical about the zero scale, and the average lift coefficient was close to zero, while the curves of the instantaneous lift coefficient of linear flapping were unbalanced.

#### 4.2. Analysis of the Influence of Flapping Mode on the Structure of the Wake Vortex of the Hydrofoil

In one period, the flapping hydrofoil will produce a counterclockwise positive vortex and a clockwise negative vortex in its wake's flow field; the former will be produced above, and the latter will be produced below the hydrofoil. This wake vortex structure is called an anti-Kármán vortex street. When the hydrofoil moves for multiple periods, multiple sets of continuous anti-Kármán vortex streets are generated in the flow field, resulting in a jet phenomenon, which is why hydrofoils can be used for water propulsion [35]. Therefore, in this section, the influence of the three flapping modes on the structure of the wake vortex is compared and analyzed using a flapping frequency of  $f = 1$  Hz.

Figure 10 shows the nephogram of the variation in the vorticity on the surface of the hydrofoil in one cycle with different flapping modes. On the basis of this comparison, it was found that during the process of the hydrofoil flapping up and down, a vortex was generated at the leading edge and trailing edge using the three hydrofoil flapping modes, and the leading-edge vortex gradually moved along the surface of the hydrofoil to the trailing edge during movement and combined with the trailing-edge vortex, before falling off at the upper and lower amplitude positions of heave. There were significant differences in the strength of leading-edge vortices of the three flapping modes of the hydrofoil in the process of flapping up and down. These occurred because, compared with linear flapping, the lateral displacement velocity of arc flapping occurs in the direction of the X axis, as shown in Figure 2, thereby changing the velocity value of the equivalent incoming flow, as shown in Equation (8), and then causing a change in the attack angle, as shown in Equation (9) and Figure 4. It is known from the literature that a change in the attack angle will affect the strength of the leading-edge vortex of the hydrofoil [23,24]. Therefore, the different flapping modes had significant effects on the generation and evolution of the leading-edge vortices.

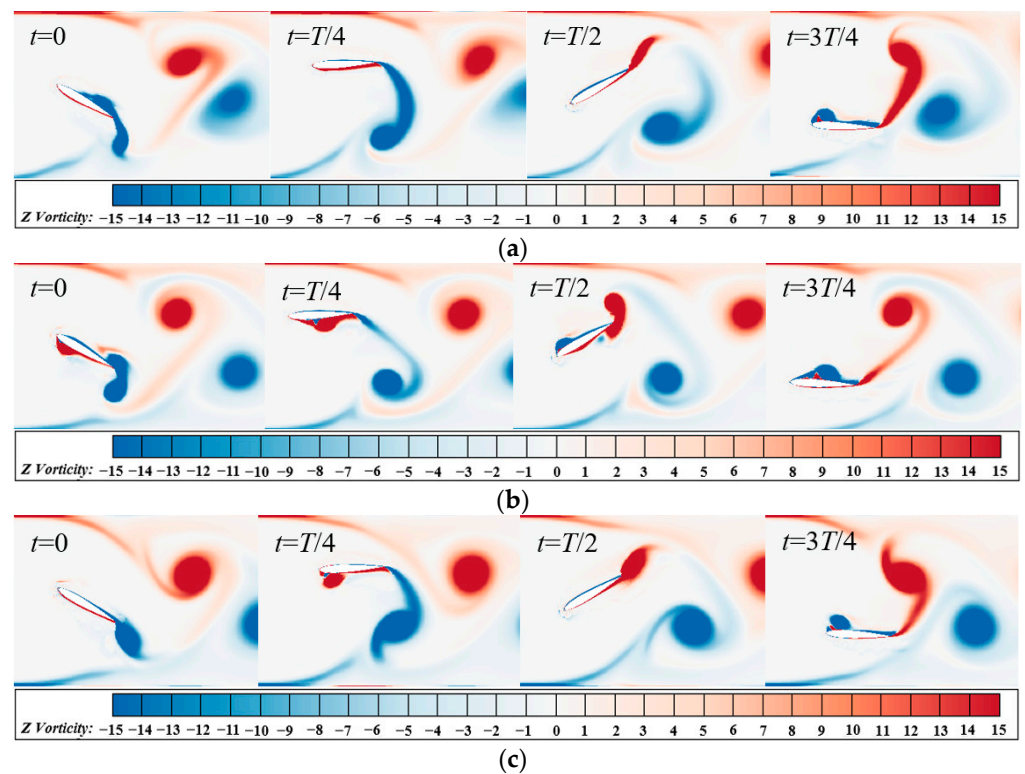


**Figure 10.** Nephogram of the change in vorticity of the hydrofoil surface in a single period under different flapping modes. (a) Linear flapping; (b) positive arc flapping; (c) negative arc flapping.

Figure 11 provides a schematic diagram of the structure of the hydrofoil's wake vortex for different flapping modes, showing that the structures of the wake vortex in three flapping modes were all anti-Kármán vortex streets, which indicates that the hydrofoil can generate a propulsion effect on the water body in the three flapping modes. However, it was found that the wake vortex of linear flapping tilted upward, and the wake vortex of positive arc flapping tended to be farther away in the flow field than that of the other two flapping modes. This is because in the process of the hydrofoil flapping up and down, the strength of the leading-edge vortex under linear flapping was very different, resulting in the strength of the positive vortex and negative vortex in the wake vortex being quite different; therefore, due to the mutual induction effect of the positive vortex and the negative vortex, and upward deflection phenomenon occurred in the wake vortex. However, in the process of the hydrofoil flapping up and down, the strength of the leading-edge vortex under the two types of arc flapping was equivalent, resulting in the strength of the positive vortex and negative vortex in the wake vortex being equal; therefore, no obvious deflection was caused by the wake vortex in either type of arc flapping. The wake vortex of positive arc flapping lasted for longer in the flow field, which may be due to the flow field velocity of positive arc flapping being greater.

It can be seen from Figures 8–11 that the instantaneous thrust coefficient is closely related to the structure of the wake vortex. The intensities of the positive vortex and negative vortex of a pair of anti-Kármán vortex streets are different, leading to the force of the vortex on the hydrofoil when it flaps up under linear flapping and the force of the vortex on the hydrofoil when it flaps down being different. Therefore, the two peaks of the instantaneous thrust coefficient of linear flapping are quite different. However, the strength of the vortex pair of the two arc flapping modes was similar, so the two thrust coefficient peaks of the two arc flapping modes showed no obvious differences.

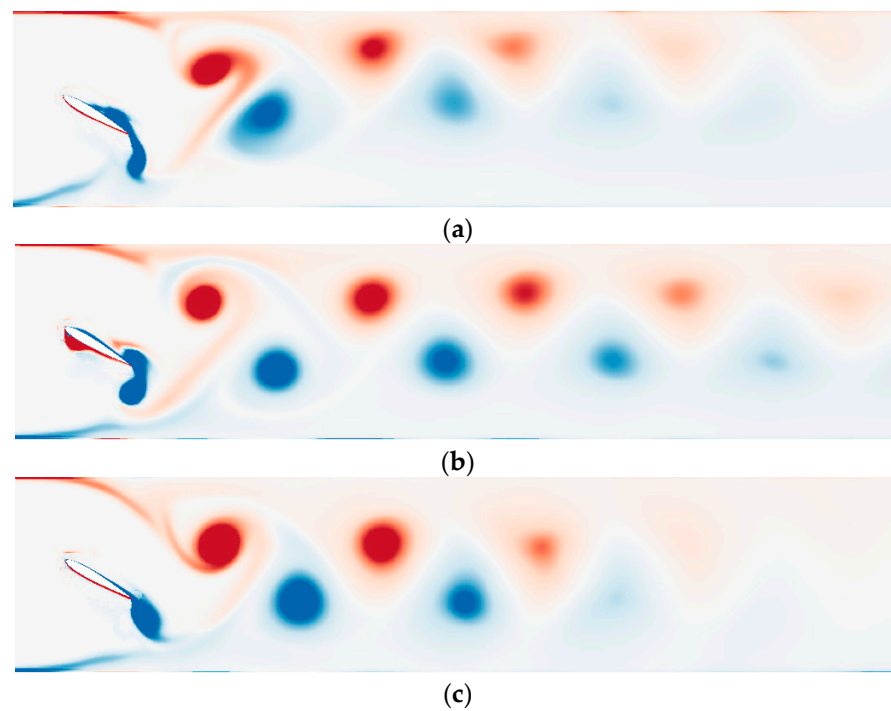


**Figure 11.** Schematic diagram of the structure of the wake vortex of a hydrofoil under different flapping modes. (a) Linear flapping; (b) positive arc flapping; (c) negative arc flapping.

#### 4.3. Analysis of the Influence of Flapping Mode on the Pumping Performance of a Hydrofoil

Different flapping modes will inevitably have different effects on water propulsion. Therefore, we used the velocity nephogram of the three flapping modes at  $f = 1$  Hz to perform a comparative analysis, as shown in Figure 12.

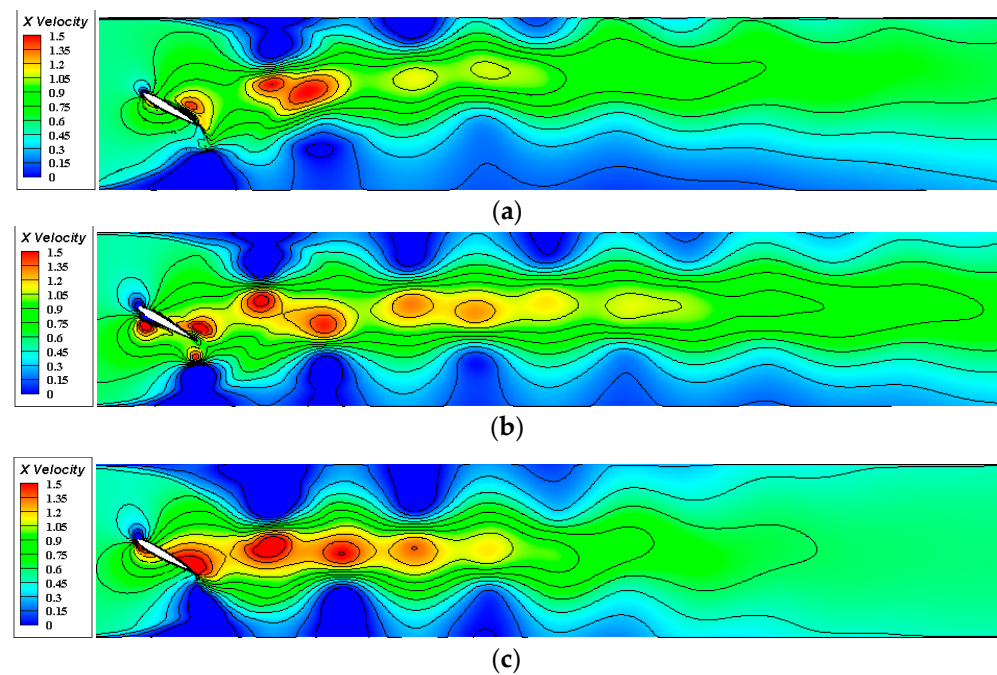


**Figure 12.** Velocity nephograms of a hydrofoil employing different flapping modes. (a) Linear flapping; (b) positive arc flapping; (c) negative arc flapping.

Figure 12 shows the velocity nephogram under the three different flapping modes. On the basis of this comparison, it was found that the forms of distribution of the three

flow fields were basically the same. The inlet on the left side of the hydrofoil was a stable incoming flow. When the incoming flow entered the range of motion of the hydrofoil, the velocity increased rapidly to form a jet, but the velocity near the wall gradually decreased, and the velocity was distributed in a gradient from the middle to both sides. With the development of the jet to the right, the jet gradually drove the low-speed water flow to the wall and formed a stable flow field. The difference was that the jet of linear flapping deflected upward, which drove the low-speed region to the upper wall, and the energy loss was high, but the jets of the two arc flapping modes were relatively vertical. In addition, in the flow field of negative arc flapping, the proportion of the low-velocity region near the wall was larger than that of the other two flapping modes, while the exit velocity of positive arc flapping was higher, and the range of the high-velocity region of the central basin was wider than that of the other two flapping modes.

In order to further study the influence of different flapping modes on the pumping efficiency of hydrofoils, a numerical simulation analysis was carried out on a hydrofoil with different flapping frequencies in the range of  $f = 0.1\text{--}5\text{ Hz}$ . The pumping efficiency of the three different flapping modes was determined, and the results are shown in Figure 13.

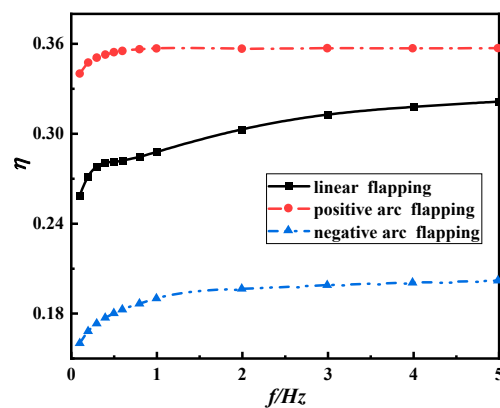


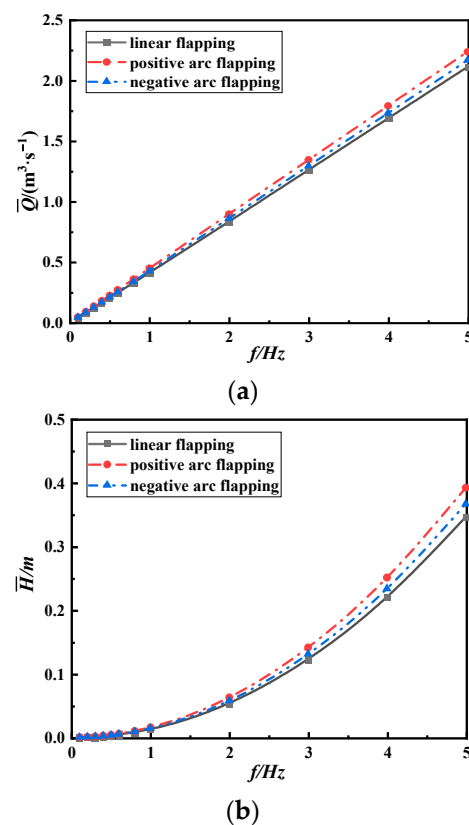
Figure 13. Pumping efficiency curves of the three flapping modes.

Figure 13 shows the curves of the water pumping efficiency of the three flapping modes under flapping frequencies ranging from 0.1 to 5 Hz. It can be clearly seen in the figure that the water pumping efficiency of the three flapping modes increased gradually with increasing flapping frequency. By comparison, the pumping efficiency of positive arc flapping was obviously higher than that of linear flapping and negative arc flapping, but that of linear flapping was higher than that of negative arc flapping.

There are two main reasons for this. On the one hand, arc flapping adds the input power in the yaw direction, and this led to an increase in the output power. However, for positive arc flapping, when the pitch angle decreased, the direction of the yaw movement was opposite to the direction of the water flow, as shown in Figure 2b ( $0 \sim T/4$ ). When the pitching angle increased, the direction of the yaw movement was the same as the direction of the water flow, as shown in Figure 2b ( $T/4 \sim T/2$ ), which led to the work done by torque at the pivot of the positive arc flapping hydrofoil being small, so the efficiency was relatively high. For negative arc flapping, when the pitch angle increased, the direction of the yaw motion was opposite to the direction of the water flow, as shown in Figure 2c ( $T/4 \sim T/2$ ). When the pitch angle decreased, the direction of the yaw motion was the same as the direction of the water flow, as shown in Figure 2c ( $0 \sim T/4$ ), leading to the work done by torque at the hydrofoil pivot being greater, but the output power increase was smaller, so the relative efficiency decreased.

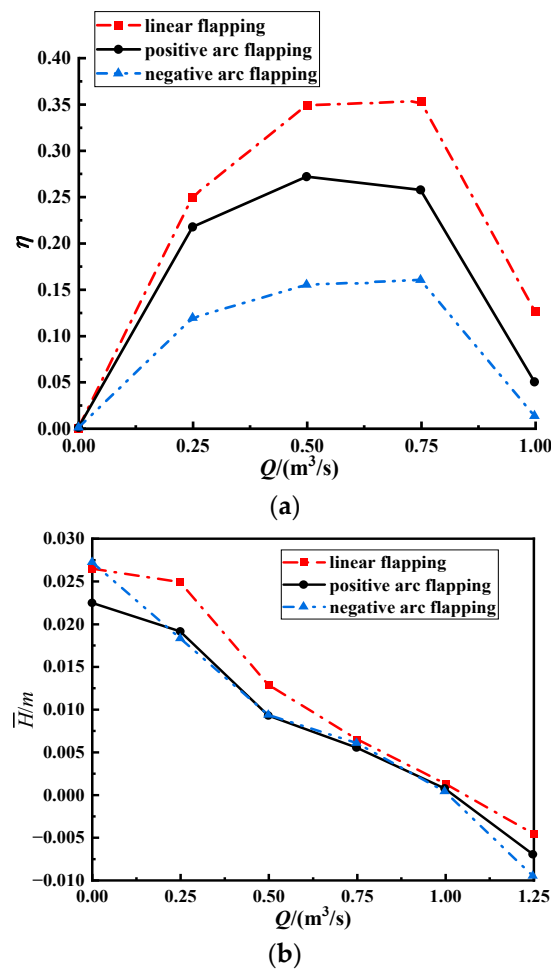
On the other hand, the wake vortex of linear flapping deflected upward and caused a loss of energy, while negative arc flapping generated resistance for a period of time, and the peak–valley value of thrust fluctuated greatly, as shown in Figure 6a, thus reducing the efficiency of the vortex energy conversion and further reducing the efficiency of pumping.

Figure 14 presents graphs showing the change in the average flow and average head for the three flapping modes with changes in flapping frequency. It can be seen from the graph that with increasing flapping frequency, the average flow increased proportionally to the flapping frequency, and the average head increased proportionally to the square of the flapping frequency. On the basis of comparison, it was found that at the same frequency, the highest average flow rate and the largest average head were obtained with positive arc flapping, while negative arc flapping ranked second, and linear flapping achieved the smallest values for these variables. In addition, changes in the flapping mode did not change the trend of the average head and the average flow rate, because all three flapping modes produced the trend of the thrust coefficient shown in Figure 8a; however, the difference was the magnitude of the average thrust.



**Figure 14.** Curve of the average flow and average head versus frequency for the three flapping modes: (a) curve of average flow vs. frequency; (b) curve of average head vs. frequency.

In order to further explore the influence of the flapping mode on the characteristic curves of the hydrofoil, the curves of efficiency and head under different flow rates were calculated by setting the velocity at the inlet. The inlet velocity varied from 0 to 1.56 m/s and the flapping frequency of the hydrofoil was set to  $f = 1$  Hz. The results are shown in Figure 15.



**Figure 15.** Characteristic curves of the hydrofoil under three flapping modes: (a) flow vs. efficiency; (b) flow vs. head.

It can be seen from Figure 15 that the characteristic curve of the flapping hydrofoil and the characteristic curve of the traditional axial flow pump had a similar change trend, namely that with increasing flow rate, the head decreased gradually, whereas the pumping efficiency first increased and then decreased, and both of them had an optimal efficiency point. This is because when the flow rate at the inlet is small, it has not yet reached the propulsion threshold of the hydrofoil, and the hydrofoil's propulsion of the water body is represented by thrust, so the pumping efficiency of the hydrofoil gradually improved. However, with a continuous increase in the flow rate until it exceeds the propulsion threshold of the hydrofoil, the thrust of the hydrofoil on the water body gradually decreases and is then converted into resistance, resulting in a decrease in the pumping efficiency of the hydrofoil, while the head is gradually reduced to a negative value.

It can be seen from the comparison in Figure 15a that, under the same flow rate, the pumping efficiency of positive arc flapping was the highest, reaching 35%, followed by linear flapping, and negative arc flapping was the least efficient. In addition, the highly efficient flow rate of linear flapping was lower than that of the other two flapping modes. As can be seen from Figure 15b, the maximum average head of the three flapping modes was 0.027 m. In addition, under conditions with the same average head, positive arc flapping had the advantage of a higher flow rate, so it was able to meet the working condition requirements of an ultra-low head.

## 5. Conclusions

In this study, a more realistic fishtail swinging mode was considered, and an arc flapping mode was proposed based on the traditional linear flapping mode. The pumping performance of a hydrofoil under three flapping modes, namely linear flapping, positive arc flapping, and negative arc flapping, was compared and analyzed by means of numerical simulation in order to provide further guidance for the structural optimization of bionic pumping devices. The conclusions are as follows:

- (1) The mechanical properties of the flapping hydrofoil were obviously affected by the different flapping modes. In one cycle of motion, the hydrofoils with positive arc flapping and linear flapping always delivered thrust to the water, but the hydrofoil with negative arc flapping produced both thrust and drag. The two peak values of the instantaneous thrust coefficient of linear flapping were different, but the two peak values of the instantaneous thrust coefficient of positive arc flapping and negative arc flapping were basically the same, so the thrust coefficient curve of the arc flapping hydrofoil was more stable compared with that of the linear flapping hydrofoil, and the peak value of positive arc flapping was 46.5% lower than that of linear flapping.
- (2) The three flapping modes all had a propulsion effect on the water flow, and the structure of the wake flow field showed anti-Kármán vortex streets. However, compared with the other two flapping modes, the wake vortex of linear flapping deflected upward in the flow field, and the wake vortex of positive arc flapping extended for a longer distance in the flow field. At the same time, the angle of attack of the hydrofoil was also affected by the different flapping modes, which further affected the formation and evolution of the leading-edge vortex.
- (3) At a fixed frequency, positive arc flapping had the greatest pumping efficiency, followed by linear flapping, and negative arc flapping was the least efficient. Moreover, compared with the other two flapping modes, the outlet flow rate of positive arc flapping was higher, and the high-speed drainage area in the center of the flow field was wider, which would be more conducive to pumping water. In addition, the flapping hydrofoil had a characteristic curve similar to that of the traditional axial flow pump, namely showing that the efficiency first increased and then decreased with increasing flow rate, and the average head decreased with increasing flow rate. The hydrofoil with positive arc flapping had a pumping efficiency of 35% when the average head was 0.013 m, which was able to adequately meet the requirements of conditions with an ultra-low head.

**Author Contributions:** E.H. presented the main idea of analyzing of pumping performance of arc and linear flapping hydrofoils; W.Z. contributed to the overall composition and the writing of the manuscript; Z.S. conducted the numerical theory research; R.X. reviewed the manuscript; H.L. provided writing ideas; L.Q. revised the manuscript. All authors have read and agreed to the published version of the manuscript.

**Funding:** This research was funded by the National Natural Science Foundation of China (Grant No. 51976202, 61772469) and the Zhejiang Provincial Key Research and Development Project (Grant No. 2021C03019) and the Zhejiang Provincial Key Laboratory of Rural Water Conservancy and Hydropower Resources Allocation and Control Key Technologies Open Fund Project (Grant No. UZJWEU-RWM-20200304B).

**Conflicts of Interest:** The authors declare no conflict of interest.

## References

1. Cai, Y. *Experimental Study on the Relationship between River Structure and Water Quality Restoration in Plain Area*; Suzhou University: Suzhou, China, 2007.
2. Phillips, J.D.; Slattery, M.C. Downstream trends in discharge, slope, and stream power in a lower coastal plain river. *J. Hydrol.* **2007**, *334*, 290–303. [[CrossRef](#)]
3. Peng, Z.; Hu, W.; Zhang, Y.; Liu, G.; Zhang, H.; Gao, R. Modelling the effects of joint operations of water transfer project and lake sluice on circulation and water quality of a large shallow lake. *J. Hydrol.* **2021**, *593*, 125881. [[CrossRef](#)]

4. Snedden, G.A.; Cable, J.E.; Swarzenski, C.; Swenson, E. Sediment discharge into a subsiding Louisiana deltaic estuary through a Mississippi River diversion. *Estuar. Coast. Shelf Sci.* **2007**, *71*, 181–193. [[CrossRef](#)]
5. Yuan, D.; Zhang, Y.J.; Liu, J.M.; Gao, S.C.; Song, X.Y. Water Quantity and Quality Joint-Operation Modeling of Dams and Floodgates in Huai River Basin, China. *J. Water Resour. Plan. Manage ASCE* **2015**, *141*, 12. [[CrossRef](#)]
6. Zuo, Z.G.; Liu, S.H. Flow-Induced Instabilities in Pump-Turbines in China. *Engineering* **2017**, *3*, 504–511. [[CrossRef](#)]
7. Feng, J.J.; Luo, X.Q.; Guo, P.C.; Wu, G.K. Influence of tip clearance on pressure fluctuations in an axial flow pump. *J. Mech. Sci. Technol.* **2016**, *30*, 1603–1610. [[CrossRef](#)]
8. Shao, X.M.; Pan, D.Y. Hydrodynamics of A Flapping Foil in The Wake of a D-Section Cylinder. *J. Hydrodyn.* **2011**, *23*, 422–430. [[CrossRef](#)]
9. Hua, E.R.; Chen, W.Q.; Tang, S.W.; Xie, R.S.; Guo, X.M.; Xu, G.H. Study on the characteristics of pushing flow of flapping hydrofoil device in small channel. *J. Agric. Mach.* **2022**, *53*, 9.
10. Hua, E.R.; Luo, H.T.; Xie, R.S.; Chen, W.Q.; Tang, S.W.; Jin, D.Y. Investigation on the Influence of Flow Passage Structure on the Performance of Bionic Pumps. *Processes* **2022**, *10*, 2569. [[CrossRef](#)]
11. Koochesfahani, M.M. Vortical patterns in the wake of an oscillating airfoil. *Aiaa J.* **1989**, *27*, 1200–1205. [[CrossRef](#)]
12. Cao, Y.H.; Chao, L.M.; Ding, H. Influence of Zhao Hongyin’s hybrid airfoil on the propulsive performance of flapping wing. *J. Shanghai Jiaotong Univ.* **2016**, *50*, 6.
13. Tian, W.; Bodling, A.; Liu, H.; Wu, J.C.; He, G.W.; Hu, H. An experimental study of the effects of pitch-pivot-point location on the propulsion performance of a pitching airfoil. *J. Fluids Struct.* **2016**, *60*, 130–142. [[CrossRef](#)]
14. Kumar, R.; Shin, H. Thrust Prediction of an Active Flapping Foil in Waves Using CFD. *J. Mar. Sci. Eng.* **2019**, *7*, 396. [[CrossRef](#)]
15. Wang, P.; Tian, X.; Lu, W.; Hu, Z.; Luo, Y. Dynamic modeling and simulations of the wave glider. *Appl. Math. Model.* **2019**, *66*, 77–96. [[CrossRef](#)]
16. Kraus, N.; Bingham, B. Estimation of wave glider dynamics for precise positioning. In Proceedings of the OCEANS’11 MTS/IEEE KONA, Waikoloa, HI, USA, 19–22 September 2011; pp. 1–9.
17. Kinsey, T.; Dumas, G. Parametric study of an oscillating airfoil in a power-extraction regime. *Aiaa J.* **2008**, *46*, 1318–1330. [[CrossRef](#)]
18. Kinsey, T.; Dumas, G.; Lalande, G.; Ruel, J.; Mehut, A.; Viarouge, P.; Lemay, J.; Jean, Y. Prototype testing of a hydrokinetic turbine based on oscillating hydrofoils. *Renew. Energy* **2011**, *36*, 1710–1718. [[CrossRef](#)]
19. Kinsey, T.; Dumas, G. Computational Fluid Dynamics Analysis of a Hydrokinetic Turbine Based on Oscillating Hydrofoils. *J. Fluids Eng. Trans. ASME* **2012**, *134*, 16. [[CrossRef](#)]
20. Huang, Y.; Zhang, J.H.; Hu, X.Q.; Xia, Q.X.; Huang, W.Q.; Zhao, C.S. Dynamics analysis and experiment on the fishtailing type of valveless piezoelectric pump with rectangular vibrator. *Sci. China-Technol. Sci.* **2010**, *53*, 3241–3247. [[CrossRef](#)]
21. Hu, X.Q.; Zhang, J.H.; Huang, Y.; Xia, Q.X.; Huang, W.Q.; Zhao, C.S. Principle and experimental verification of caudal-fin-type piezoelectric-stack pump with variable-cross-section oscillating vibrator. *Chin. J. Mech. Eng.* **2012**, *25*, 128–136. [[CrossRef](#)]
22. Andersen, A.; Bohr, T.; Schnipper, T.; Walther, J.H. Wake structure and thrust generation of a flapping foil in two-dimensional flow. *J. Fluid Mech.* **2017**, *812*, 12. [[CrossRef](#)]
23. Wang, Z.; Song, H.J.; Yin, X.Z. Vortex field visualization of unsteady motion of two-dimensional wing. *Exp. Fluid Mech.* **2004**, *18*, 71–76.
24. Wang, Z.; Song, H.J.; Yin, X.Z. Vortex flow visualization of unsteady motion of two-dimensional airfoil–2 pitching motion and combined heaving/pitching motion. *Exp. Fluid Mech.* **2004**, *18*, 38–42.
25. Abbaspour, M.; Ebrahimi, M. Comparative numerical analysis of the flow pattern and performance of a foil in flapping and undulating oscillations. *J. Mar. Sci. Technol.* **2015**, *20*, 257–277. [[CrossRef](#)]
26. Du, X.X.; Zhang, Z.D. Numerical analysis of the influence of four flapping modes on the propulsive performance of underwater flapping wing. *Eng. Mech.* **2018**, *35*, 8.
27. Feng, Y.K.; Su, Y.M.; Su, Y.Y.; Liu, H.X. Study on hydrodynamic performance of swing wing in fish-like swimming mode. *J. Huazhong Univ. Sci. Technol. Nat. Sci. Ed.* **2019**, *6*, 38–43.
28. Ma, P.L.; Wang, Y.; Liu, H.B. Hydrodynamic performance analysis of xie yudong oscillating hydrofoil. *J. Sol. Energy* **2018**, *39*, 8.
29. Lu, K.; Xie, Y.H.; Zhang, D. Numerical study of large amplitude, nonsinusoidal motion and camber effects on pitching airfoil propulsion. *J. Fluids Struct.* **2013**, *36*, 184–194. [[CrossRef](#)]
30. Lu, K.; Xie, Y.H.; Zhang, D. Nonsinusoidal motion effects on energy extraction performance of a flapping foil. *Renew. Energy* **2014**, *64*, 283–293. [[CrossRef](#)]
31. Boudis, A.; Bayeul-Laine, A.C.; Benzaoui, A.; Oualli, H.; Guerri, O.; Coutier-Delgosha, O. Numerical Investigation of the Effects of Nonsinusoidal Motion Trajectory on the Propulsion Mechanisms of a Flapping Airfoil. *J. Fluids Eng. Trans. ASME* **2019**, *141*, 18. [[CrossRef](#)]
32. Breder, C.M. The locomotion of fishes. *Zoologica* **1926**, *4*, 159–297. [[CrossRef](#)]
33. Sfakiotakis, M.; Lane, D.M.; Davies, J.B.C. Review of fish swimming modes for aquatic locomotion. *IEEE J. Ocean. Eng.* **1999**, *24*, 237–252. [[CrossRef](#)]

34. Read, D.A.; Hover, F.S.; Triantafyllou, M.S. Forces on oscillating foils for propulsion and maneuvering. *J. Fluids Struct.* **2003**, *17*, 163–183. [[CrossRef](#)]
35. Karman, T.V. General aerodynamic theory. *Perfect Fluids. Aerodyn. Theory* **1963**, *2*, 328–336.

**Disclaimer/Publisher’s Note:** The statements, opinions and data contained in all publications are solely those of the individual author(s) and contributor(s) and not of MDPI and/or the editor(s). MDPI and/or the editor(s) disclaim responsibility for any injury to people or property resulting from any ideas, methods, instructions or products referred to in the content.